

Strain-tuned structural, electronic, and superconducting properties of thin-film $\text{La}_3\text{Ni}_2\text{O}_7$

Sreekar Bheemavarapu
(Dated: December 30, 2025)

The recent discovery of high-temperature superconductivity in $\text{La}_3\text{Ni}_2\text{O}_7$ under ambient-pressure in strained thin films raises the question of how superconductivity can be optimized through strain. In this work, we investigate the strain-dependent electronic structure and superconducting transition temperature (T_c) of $\text{La}_3\text{Ni}_2\text{O}_7$ using density functional theory combined with random phase approximation spin-fluctuation calculations. We find that biaxial strain acts as a tuning parameter for Fermi surface topology and magnetic correlations. Large tensile strain drives a Lifshitz transition characterized by a d_{z^2} band crossing, leading to a sharp increase in the density of states and theoretical pairing strength. However, this is accompanied by a large increase in magnetic proximity, suggesting strong competition with spin-density-wave order. Conversely, under compressive strain, we identify a structurally selective T_c enhancement restricted to the high-symmetry $I4/mmm$ phase. This effect is driven by the straightening of Ni–O–Ni bonds and the emergence of a Γ -centered hole pocket, yielding T_c values consistent with recent thin-film experiments. Our results highlight the balance between structural symmetry, electronic topology, and magnetic instability in nickelates, and provides a theoretical framework for optimizing superconductivity via strain engineering.

I. INTRODUCTION

Nickelates have long been explored as potential analogs to cuprate high- T_c superconductors [1–4]. While superconductivity was demonstrated in infinite-layer nickelates ($R\text{NiO}_2$), critical temperatures were modest ($T_c \sim 9$ – 15 K) and synthesis proved challenging [3]. Recently, the bilayer Ruddlesden-Popper nickelate $\text{La}_3\text{Ni}_2\text{O}_7$ has attracted attention for superconducting signatures near 80 K under high hydrostatic pressure [4–6].

However, the bulk high- T_c state requires high hydrostatic pressure ($\gtrsim 14$ GPa) to suppress a competing density-wave order [4, 5, 7–9]. This requirement limits applications and complicates experimental probes like ARPES or STM. Thus, the recent discovery that epitaxial strain in thin films can stabilize ambient-pressure superconductivity with onset T_c between 26–42 K has led to much interest on the structural, electronic, and superconducting properties of thin film $\text{La}_3\text{Ni}_2\text{O}_7$ [10–14].

Strain mimics some effects of hydrostatic pressure, but introduces distinct interface and symmetry effects [10, 11, 15, 16]. In addition, unlike the nominal $3d^9$ configuration of infinite-layer nickelates, $\text{La}_3\text{Ni}_2\text{O}_7$ possesses a $3d^{7.5}$ mixed-valence state, with its physics defined by the combination of the $d_{x^2-y^2}$ orbital (intralayer hopping) and the d_{z^2} orbital, which forms strong interlayer bands via the apical oxygen [17–20]. These traits and others distinguish thin film $\text{La}_3\text{Ni}_2\text{O}_7$ from its previously studied variants.

In the bulk, superconductivity coincides with a structural transition from orthorhombic $Amam$ to higher-symmetry $Fmmm$ or $I4/mmm$ phases, although samples often contain mixed phases [21–23]. Straightening the Ni–O–Ni bond angles, particularly along the c -axis, is believed to maximize the superexchange interaction J_\perp [24, 25]. Oxygen nonstoichiometry and intergrowths further complicate interpretation [10, 21]. Evidence suggests superconductivity is mediated by spin

fluctuations [26], with strong Hund’s coupling locking orbital spins to facilitate interlayer pairing [27, 28].

The necessity of the d_{z^2} -derived hole pocket (γ pocket) crossing the Fermi level for superconductivity remains debated [29, 30]. While some models suggest this metallization is essential, recent thin-film works report superconductivity even when this band remains occupied [12, 15]. Competition between d -wave and s_\pm -wave pairing symmetries is also unresolved [31]. While s_\pm is favored by strong interlayer coupling (J_\perp), strain-tunable crystal field splitting may drive a transition to d -wave or $d + is$ states [32–34].

In this study, we use Density Functional Theory (DFT) and Wannier90 [35, 36] to construct multi-orbital tight binding models, which are then used with the Random Phase Approximation (RPA) to solve the linearized Eliashberg equation and calculate the pairing eigenvalue λ , eventually determining quantitative T_c estimates [37]. We map out the structural and electronic evolution of $\text{La}_3\text{Ni}_2\text{O}_7$ under three phases ($Amam$, $Amam$ with constrained in-plane lattice parameters, and $I4/mmm$) across a range of biaxial strains (-2.5% to $+2.0\%$). Our results reveal the interplay between strain and the structural symmetry, electronic topology, and magnetic fluctuations that govern superconductivity in $\text{La}_3\text{Ni}_2\text{O}_7$ [19, 25, 26].

II. COMPUTATIONAL METHODS

A. DFT Structural Relaxation

We studied the structural response of $\text{La}_3\text{Ni}_2\text{O}_7$ to biaxial strain for three phases: $Amam$, $Amam$ with constrained in-plane lattice parameters ($a = b$), and $I4/mmm$. All calculations used a 24-atom simulation cell. The $Amam$ phases employed a rotated $\sqrt{2} \times \sqrt{2}$ supercell, while the $I4/mmm$ phase used a conventional

cell.

The unstrained $Amam$ reference was obtained by full variable-cell relaxation of the experimental structure [38]. The $Amam$ ($a = b$) reference enforced equal in-plane parameters ($a' = b' = \sqrt{ab}$), relaxing only the c -axis and internal coordinates. The $I4/mmm$ reference was initialized from experiment [39] with in-plane parameters matched to the $Amam$ ($a = b$) reference ($a_{I4} = a_{Amam}/\sqrt{2}$), followed by relaxation of the c -axis and internal coordinates.

Biaxial strain was applied by fixing in-plane parameters ($a = (1 + \epsilon)a_0$, $b = (1 + \epsilon)b_0$) and relaxing the c -axis and internal coordinates. We considered strains $\epsilon \in \{-2.5\%, -2.0\%, -1.5\%, -1.0\%, -0.5\%, 0\%, +1.0\%, +2.0\%\}$.

B. Electronic Structure Calculations

DFT calculations were performed using QUANTUM ESPRESSO [35, 40] in the nonmagnetic state. We employed the DFT+ U formalism [41, 42] with $U_{Ni-d} = 3.5$ eV, consistent with prior studies [12, 20]. We used GBRV PBE pseudopotentials [43, 44] with a 40 Ry kinetic energy cutoff and 320 Ry charge density cutoff. Occupations were treated with Marzari-Vanderbilt cold smearing [45] (width 0.02 Ry). The energy convergence threshold was 10^{-8} Ry.

Relaxations used a $10 \times 10 \times 5$ k-mesh for $Amam$ phases and $12 \times 12 \times 4$ for $I4/mmm$. Self-consistent calculations used $12 \times 12 \times 6$ ($Amam$) and $17 \times 17 \times 4$ ($I4/mmm$) meshes to maintain comparable sampling density. Non-self-consistent calculations used $16 \times 16 \times 8$ ($Amam$) and $22 \times 22 \times 4$ ($I4/mmm$) meshes.

C. Wannierization

Maximally localized Wannier functions were constructed via WANNIER90 [36, 46] using a minimal two-orbital Ni e_g model (d_{z^2} , $d_{x^2-y^2}$) [17]. We used a disentanglement window of ($E_F - 2$ eV, $E_F + 3.5$ eV) and a frozen window of ($E_F - 1.0$ eV, $E_F + 1.0$ eV) across all strains and phases.

D. Susceptibility and RPA Formalism

Multi-orbital susceptibility was calculated from the Wannier models. The bare susceptibility $\chi_0^{pqrs}(\mathbf{q})$ was computed on a 64×64 \mathbf{q} -mesh using a 64×64 \mathbf{k} -mesh and broadening $\eta = 2$ meV, including temperature dependence via Fermi-Dirac distributions:

$$\chi_0^{pqrs}(\mathbf{q}) = -\frac{1}{N_k} \sum_{\mathbf{k}, \mu, \nu} \frac{f(E_\nu(\mathbf{k} + \mathbf{q})) - f(E_\mu(\mathbf{k}))}{E_\nu(\mathbf{k} + \mathbf{q}) - E_\mu(\mathbf{k}) + i\eta} \quad (1)$$

$$\times U_\mu^p(\mathbf{k})^* U_\mu^q(\mathbf{k}) U_\nu^r(\mathbf{k} + \mathbf{q})^* U_\nu^s(\mathbf{k} + \mathbf{q})$$

where $E_\mu(\mathbf{k})$ and $U_\mu^p(\mathbf{k})$ are eigenvalues and eigenvectors, and $f(E)$ is the Fermi-Dirac distribution.

Spin (χ_s) and charge (χ_c) susceptibilities were obtained in the random phase approximation (RPA):

$$\chi_s^{RPA}(\mathbf{q}) = \chi_0(\mathbf{q})[1 - U_s \chi_0(\mathbf{q})]^{-1} \quad (2)$$

$$\chi_c^{RPA}(\mathbf{q}) = \chi_0(\mathbf{q})[1 + U_c \chi_0(\mathbf{q})]^{-1} \quad (3)$$

where U_s and U_c are orbital-space interaction matrices including intra-orbital U , inter-orbital U' , Hund's coupling J , and pair hopping J' ($U' = U - 2J$, $J' = J$). Note that this U differs from the DFT+ U one, being a low-energy effective interaction. We determined the interaction strength U using a Stoner criterion: for each structure, U was set to $0.99U_{crit}$, where U_{crit} is the critical value for magnetic instability (i.e. the U that makes the largest eigenvalue of $U_s \chi_0(\mathbf{q})$ equal 1), with fixed $J/U = 0.15$.

The singlet pairing vertex $\Gamma(\mathbf{k}, \mathbf{k}')$ was constructed from spin and charge fluctuations:

$$\Gamma(\mathbf{q}) = \frac{3}{2} U_s \chi_s^{RPA}(\mathbf{q}) U_s - \frac{1}{2} U_c \chi_c^{RPA}(\mathbf{q}) U_c + \frac{1}{2} (U_s + U_c) \quad (4)$$

where $\mathbf{q} = \mathbf{k} - \mathbf{k}'$. We also included the symmetric $\Gamma(\mathbf{k} + \mathbf{k}')$ contribution. We maintained a fixed filling of $n = 1.5$ electrons per Ni site across all strains and phases by adjusting the chemical potential.

E. T_c Estimation

T_c was determined by solving the linearized Eliashberg gap equation. The Fermi surface was discretized using k-points within $|E_n(\mathbf{k}) - \mu| < 5$ meV, subsampled to 600-1600 points if necessary. Integration weights $w_i = \Delta l_i / (2\pi v_F(\mathbf{k}_i))$ were assigned using an arc-length method. The gap equation $\lambda \Delta(\mathbf{k}) = -\sum_{\mathbf{k}'} \Gamma(\mathbf{k}, \mathbf{k}') w_{\mathbf{k}'} \Delta(\mathbf{k}')$ was solved by symmetrizing the kernel $\tilde{\Gamma}_{ij} = \sqrt{w_i} \Gamma_{ij} \sqrt{w_j}$. We included a logarithmic cutoff factor $\ln(1.13\omega_c/T)$ with $\omega_c = 60$ meV. T_c is defined as the temperature where the leading eigenvalue $\lambda = 1$.

III. RESULTS

A. Structural energetics under biaxial strain

Figure 1 shows the total energy vs. biaxial strain for each phase, referenced to the lowest energy strain/phase (unstrained $Amam$). Energy differences are ~ 10 meV/f.u. The $Amam$ and $Amam$ ($a = b$) curves are nearly identical, indicating a low energy cost for enforcing in-plane tetragonality. The $I4/mmm$ phase remains higher in energy throughout, but becomes competitive with the $Amam$ phases under large compressive strain. On the other hand, tensile strain stabilizes the lower-symmetry phases, increasing the energy difference between the $Amam$ phases and $I4/mmm$.

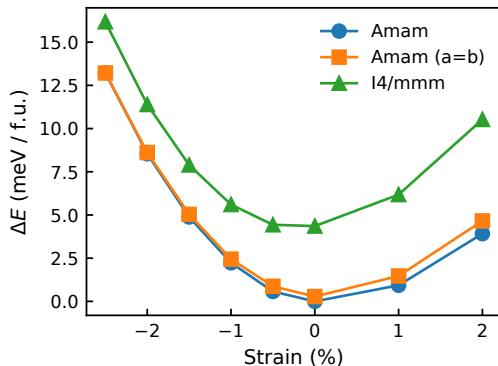


FIG. 1. Total energy as a function of biaxial strain for each phase, referenced to the minimum-energy structure (unstrained $Amam$). Energy differences remain on the order of 10 meV/f.u. across the strain range shown.

B. Structural response to biaxial strain

Figure 2 shows the evolution of the out-of-plane lattice parameter c and in-plane Ni–O–Ni bond angle. c decreases linearly from compressive to tensile strain, consistent with a Poisson response. As expected, the Ni–O–Ni bond angle decreases with tensile strain, indicating enhanced octahedral tilting, while compressive strain straightens the bonds [12, 14]. $Amam$ and $Amam (a=b)$ trends are similar, with only modest differences throughout. In $I4/mmm$, the angle is fixed at 180° by symmetry. Consistent with Ref. [12], the $Amam$ bond angles do not fully straighten to 180° even under large compression.

C. Electronic structure and low-energy spectral weight

1. Wannier and DFT band structures

Figure 3 compares DFT and Wannier bands at -2.0% strain, showing excellent agreement near the Fermi level. A gap around -1.2 eV separates bonding states from the Ni e_g manifold.

Figure 4 shows the Wannier band evolution. Note that $Amam$ calculations used a rotated supercell, folding the $I4/mmm$ zone-corner M point to Γ . The $d_{x^2-y^2}$ bands are identified by their large in-plane bandwidth, while the d_{z^2} bands appear as bonding–antibonding pairs with comparable in-plane dispersion but sizable energy splitting arising from bilayer coupling.

2. Density of states at the Fermi level

Figure 5 shows the strain dependence of the density of states at the Fermi level, $N(E_F)$. $N(E_F)$ evolves non-monotonically, with a sharp rise at large tensile strain

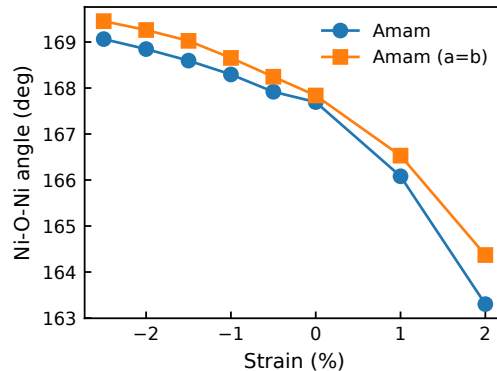
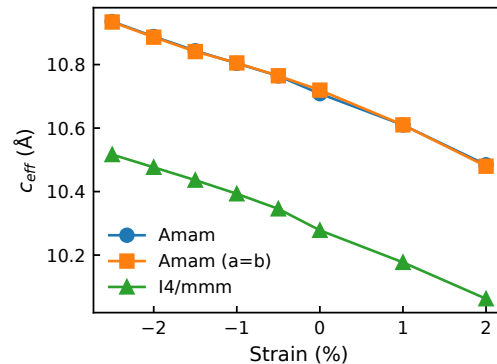


FIG. 2. Evolution of the out-of-plane lattice parameter c (top) and the in-plane Ni–O–Ni bond angle (bottom) for the strained structures. The out-of-plane parameter decreases as strain is tuned from compressive to tensile values, while the bond angle decreases with increasing tensile strain. The bond angle for the $I4/mmm$ phase (not shown) is fixed at 180° by symmetry.

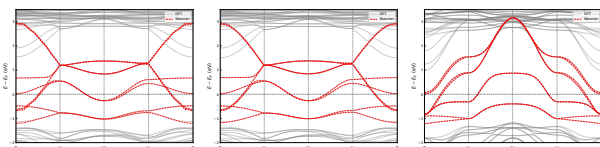


FIG. 3. Representative validation at -2.0% strain, comparing DFT bands (black) to the Wannier interpolation (red dashed) near the Fermi level for $Amam$ (left), $Amam (a=b)$ (center), and $I4/mmm$ (right).

across all phases. This increase is likely driven by a Lifshitz transition where a Ni d_{z^2} bonding band crosses the Fermi level (at M in $I4/mmm$, Γ in $Amam$), as seen in Figure 4. There is also a modest increase in $N(E_F)$ under compressive strain for the $Amam$ phases, likely due to a different band approaching E_f near Γ .

3. Fermi surface evolution

At zero strain, all phases show a central pocket and quasi-1D sheets (Fig. 6). Under compression, $I4/mmm$

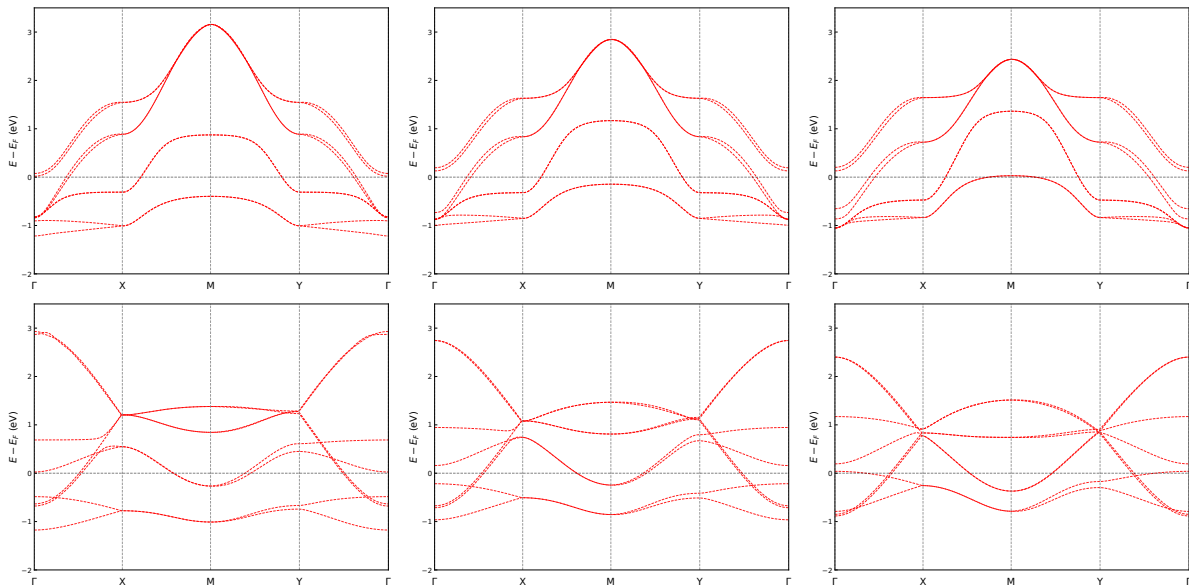


FIG. 4. Wannier band structures for the $I4/mmm$ phase (top row) and $Amam$ ($a = b$) phase (bottom row) under biaxial strain. Columns correspond to -2.0% (compressive), 0% (unstrained), and $+2.0\%$ (tensile) strain. The Fermi level is at 0 eV. Note that because of the skewed and rotated $Amam$ cell, the bands do not cleanly align with the $I4/mmm$ bands.

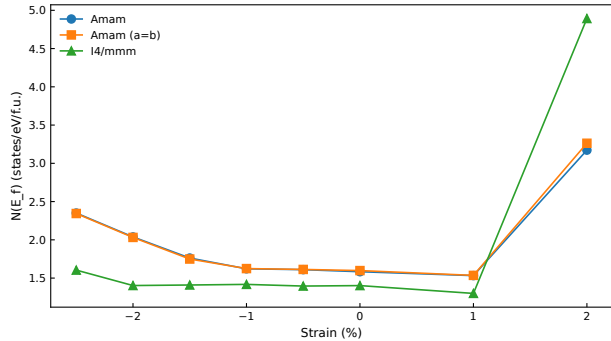


FIG. 5. Strain dependence of the density of states at the Fermi level, $N(E_F)$. A nonmonotonic evolution is observed, with a sharp rise at large tensile strain.

develops a small Γ -centered pocket (Fig. 7), arising from a shift of the chemical potential at fixed filling that drives a d_{z^2} -derived band to cross the Fermi level. Under large tensile strain, all phases undergo a Lifshitz transition, with new pockets emerging near the zone corners (M points).

D. Magnetic proximity under biaxial strain

Figure 8 shows the critical interaction strength U_c for magnetic instability (defined so that the largest eigenvalue of $U_s \chi_0(\mathbf{q})$ at $U = U_c$ equals 1). U_c generally decreases from compressive to tensile strain, indicating enhanced magnetic proximity under tensile strains, which are likely closer to spin-density-wave instabilities [4, 8].

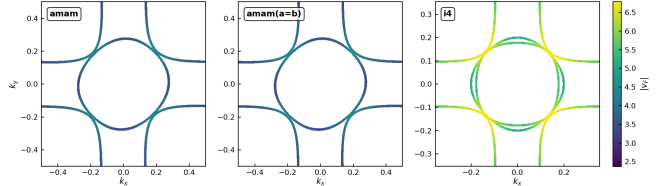


FIG. 6. Fermi surface comparison at 0% strain for $Amam$ (left), $Amam$ ($a = b$) (center), and $I4/mmm$ (right). Note that the $I4/mmm$ phase has been zoomed in to match the $Amam$ supercell, and that the $Amam$ phases have been rotated to align with the $I4/mmm$ axes.

E. T_c evolution under biaxial strain

Figure 9 illustrates T_c determination for $I4/mmm$ at -2.0% strain. Figure 10 summarizes T_c vs. strain. Large tensile strain strongly enhances T_c across all phases, coinciding with the Lifshitz transition and increased spectral weight. This large value is likely an overestimate caused by limitations of the model (e.g. neglected strong-coupling effects and competing order), but qualitatively agrees with prior theoretical works [15, 19, 25]. $I4/mmm$ also shows moderate enhancement under compression (≈ 32 K at -1.0% , ≈ 27 K at -2.0%), comparable to experimental values (≈ 26 - 42 K) [10]. This suggests our framework captures key aspects of strain-dependent superconductivity in $La_3Ni_2O_7$.

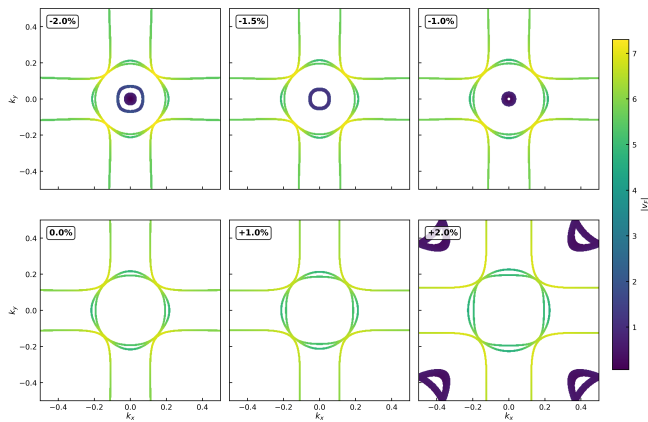


FIG. 7. Fermi surface evolution of the $I4/mmm$ phase under selected strains. Under compressive strain, a small Γ -centered pocket appears due to a strain-induced band crossing at the Fermi level. This pocket vanishes near zero strain. At +2.0% tensile strain, a Lifshitz transition occurs, with new pockets emerging near the Brillouin-zone corners (M points).

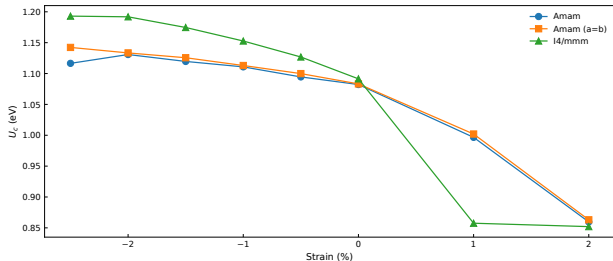


FIG. 8. Strain dependence of U_c , defined as the interaction strength U at which the leading magnetic eigenmode reaches the Stoner instability condition. Smaller U_c corresponds to stronger magnetic tendency.

1. Robustness of results

We tested robustness against variations in Hubbard U , k -mesh density, smearing, Wannier windows, and filling. The trends of tensile enhancement and, for $I4/mmm$, compressive increase, remained consistent, suggesting that they are robust features of the model.

IV. DISCUSSION

Our results demonstrate that strain acts as a tuning parameter that changes the balance between structural symmetry, electronic topology, and magnetic proximity, rather than simply modifying bandwidths. The small energy separation between the $Amam$, $Amam (a = b)$, and $I4/mmm$ phases (Fig. 1) indicates that multiple structural phases are experimentally accessible, particularly in thin-film geometries, and that superconductivity does not strictly require the global energy minimum structure, consistent with observations of mixed-phase sam-

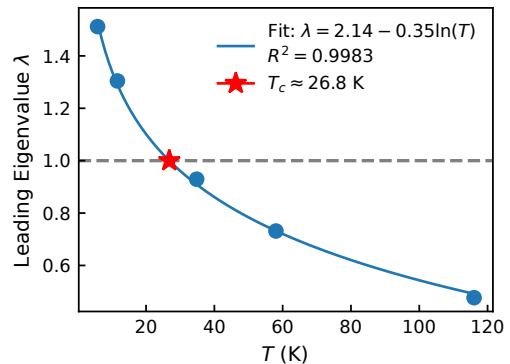


FIG. 9. Temperature dependence of the leading pairing eigenvalue λ for the $I4/mmm$ phase at -2.0% strain. The solid line represents a logarithmic fit $\lambda = A + B \ln(T)$, used to determine T_c at $\lambda = 1$.

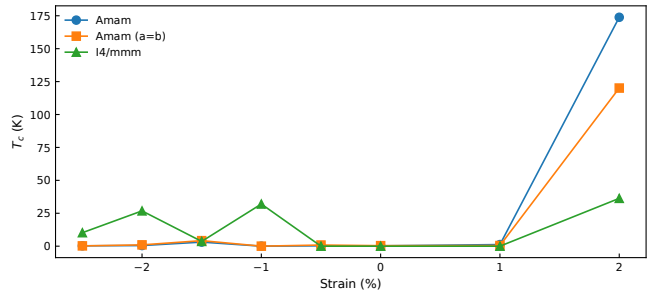


FIG. 10. T_c vs. strain for $Amam$, $Amam (a = b)$, and $I4/mmm$ phases. A pronounced enhancement of T_c is observed at large tensile strains for all structural paths, coinciding with a Lifshitz transition in the Fermi surface. In addition, the $I4/mmm$ phase exhibits a moderate T_c enhancement under certain compressive strains.

ples [21–23]. Notably, the near-degeneracy of the $Amam$ and $Amam (a = b)$ phases suggests that enforcing in-plane tetragonality alone has little effect on the pairing tendency, implying that static crystal symmetry is not a dominant factor. At the same time, compressive strain significantly lowers the energetic penalty of the high-symmetry $I4/mmm$ phase while straightening the Ni–O–Ni bonds (Fig. 2), thereby enhancing interlayer superexchange and stabilizing electronic features associated with pressure-induced superconductivity, as discussed in Refs. [12, 14].

Electronically, strain primarily tunes the relative position and occupation of the Ni d_{z^2} states, while the $d_{x^2-y^2}$ bands remain broadly dispersive and quasi-two-dimensional across all strain values (Fig. 4). Under tensile strain, a d_{z^2} -derived bonding band crosses the Fermi level, producing a Lifshitz transition that sharply increases the low-energy spectral weight, similar to findings in Refs. [15, 29]. Consequently, the density of states at the Fermi level, $N(E_F)$, exhibits a nonmonotonic evolution directly tied to changes in Fermi surface topology

rather than gradual band renormalization (Fig. 5). While the specific location of the emergent pocket depends on crystal symmetry (M point in $I4/mmm$, Γ in folded $Amam$), its physical role of introducing additional d_{z^2} character near the Fermi level is consistent across phases. Conversely, under compressive strain in the $I4/mmm$ phase, a small Γ -centered pocket appears (Fig. 7), leading to a more modest enhancement of $N(E_F)$. Notably, this pocket arises from a shift in chemical potential at fixed filling, suggesting that doping may be an interesting pathway to further tune superconductivity.

Tensile strain strongly enhances T_c in our calculations by driving a Lifshitz transition that increases low-energy spectral weight and amplifies spin fluctuations through improved nesting conditions, consistent with theoretical proposals for the bulk material [19, 25]. However, tensile strain also produces a large reduction in the critical interaction strength U_c (Fig. 8), indicating increased magnetic proximity and likely bringing the system close to a competing spin-density-wave instability, in agreement with reports of magnetic order in the parent compounds [8, 26]. As a result, superconductivity under tensile strain may be strongly constrained by competition with magnetic order, potentially explaining why tensile-strained samples do not exhibit superconductivity in experiment [13] despite the large pairing strength predicted here and in other theoretical studies [15]. The similar T_c trends for $Amam$ and $Amam$ ($a = b$) further reinforce that superconductivity is primarily governed by electronic structure evolution rather than structural details.

Crucially, the moderate T_c enhancement found under compressive strain in the $I4/mmm$ phase aligns with experimental observations in strained thin films [10, 11, 13]. This effect is structurally selective: in the high-symmetry $I4/mmm$ phase, straight Ni–O–Ni bonds allow compression to enhance interlayer coupling, driving a d_{z^2} -derived band across the chemical potential. This creates a small Γ -centered hole pocket (Fig. 7), appearing in our calculations due to the fixed filling constraint ($n = 1.5$)—which increases low-energy spectral weight and spin fluctuations. Conversely, octahedral tilting in the $Amam$ phases limits interlayer coupling, preventing the formation of this pocket and suppressing T_c enhancement. These findings support

a spin-fluctuation-mediated pairing mechanism where d_{z^2} metallization, while not necessarily required, significantly boosts pairing, consistent with recent work on the γ pocket [15, 29]. Overall, the agreement between our calculated and experimental T_c values suggests that our framework captures the essential physics of strain-tuned superconductivity in $\text{La}_3\text{Ni}_2\text{O}_7$.

V. CONCLUSION

In summary, we have theoretically investigated the strain dependence of superconductivity in $\text{La}_3\text{Ni}_2\text{O}_7$ using a combined DFT+ U and RPA spin-fluctuation framework. Our results reveal a nonmonotonic evolution of T_c driven by the interactions between structural symmetry, electronic topology, and magnetic correlations. We find that large tensile strain induces a Lifshitz transition, which is characterized by a Ni d_{z^2} band crossing the Fermi level. This transition sharply increases the density of states and spin fluctuations, theoretically enhancing T_c . However, this regime is also accompanied by a strong increase in magnetic proximity, suggesting that competing spin-density-wave order may suppress superconductivity in experiments.

Under compressive strain, we identify a structurally selective enhancement of T_c specific to the high-symmetry $I4/mmm$ phase. This effect arises from the formation of a small Γ -centered hole pocket (γ pocket), boosting interlayer coupling. The resulting moderate T_c enhancement aligns well with experimental observations in compressively strained thin films, highlighting the critical role of the γ pocket in optimizing pairing. Our findings demonstrate that strain is an effective tuning parameter for nickelate superconductivity, capable of manipulating Fermi surface topology and magnetic competition to access higher transition temperatures. These insights suggest that stabilizing the $I4/mmm$ phase under moderate compressive strain or doping to tune the γ pocket occupancy offer promising routes for optimizing ambient-pressure superconductivity in $\text{La}_3\text{Ni}_2\text{O}_7$.

VI. DATA AVAILABILITY

The data and code supporting the findings of this study are available from the author upon reasonable request.

-
- [1] V. I. Anisimov, D. Bukhvalov, and T. M. Rice, *Physical Review B* **59**, 7901 (1999).
 - [2] K.-W. Lee and W. E. Pickett, *Physical Review B* **70**, 165109 (2004).
 - [3] D. Li, K. Lee, B. Y. Wang, M. Osada, S. Crossley, H. R. Lee, Y. Cui, Y. Hikita, and H. Y. Hwang, *Nature* **572**, 624 (2019).
 - [4] H. Sun, M. Huo, X. Hu, J. Li, Z. Liu, Y. Han, L. Tang, Z. Mao, P. Yang, B. Wang, J. Cheng, D.-X. Yao, G.-M.

- Zhang, and M. Wang, *Nature* **621**, 493 (2023).
- [5] G. Wang, N. N. Wang, X. L. Shen, J. Hou, L. Ma, L. F. Shi, Z. A. Ren, Y. D. Gu, H. M. Ma, P. T. Yang, Z. Y. Liu, H. Z. Guo, J. P. Sun, G. M. Zhang, S. Calder, J.-Q. Yan, B. S. Wang, Y. Uwatoko, and J.-G. Cheng, *Physical Review X* **14**, 011040 (2024).
- [6] J. Hou, P.-T. Yang, Z.-Y. Liu, J.-Y. Li, P.-F. Shan, L. Ma, G. Wang, N.-N. Wang, H.-Z. Guo, J.-P. Sun, Y. Uwatoko, M. Wang, G.-M. Zhang, B.-S. Wang, and

- J.-G. Cheng, *Chinese Physics Letters* **40**, 117302 (2023).
- [7] Y. Zhang, D. Su, Y. Huang, Z. Shan, H. Sun, M. Huo, K. Ye, J. Zhang, Z. Yang, Y. Xu, Y. Su, R. Li, M. Smidman, M. Wang, L. Jiao, and H. Yuan, *Nature Physics* **20**, 1269 (2024).
- [8] Z. Liu, H. Sun, M. Huo, X. Ma, Y. Ji, E. Yi, L. Li, H. Liu, J. Yu, Z. Zhang, Z. Chen, F. Liang, H. Dong, H. Guo, D. Zhong, B. Shen, S. Li, and M. Wang, *Science China Physics, Mechanics & Astronomy* **66**, 217411 (2022).
- [9] K. Chen, X. Liu, J. Jiao, M. Zou, C. Jiang, X. Li, Y. Luo, Q. Wu, N. Zhang, Y. Guo, and L. Shu, *Physical Review Letters* **132**, 256503 (2024).
- [10] E. K. Ko, Y. Yu, Y. Liu, L. Bhatt, J. Li, V. Thampy, C.-T. Kuo, B. Y. Wang, Y. Lee, K. Lee, J.-S. Lee, B. H. Goodge, D. A. Muller, and H. Y. Hwang, *Nature* **638**, 935 (2025).
- [11] G. Zhou, W. Lv, H. Wang, Z. Nie, Y. Chen, Y. Li, H. Huang, W.-Q. Chen, Y.-J. Sun, Q.-K. Xue, and Z. Chen, *Nature* **640**, 641 (2025).
- [12] H. C. R. B. Bhatta, X. Zhang, Y. Zhong, and C. Jia, *Structural and Electronic Evolution of Bilayer Nickelates Under Biaxial Strain* (2025), arXiv:2502.01624 [cond-mat].
- [13] M. Osada, C. Terakura, A. Kikkawa, M. Nakajima, H.-Y. Chen, Y. Nomura, Y. Tokura, and A. Tsukazaki, *Communications Physics* **8**, 251 (2025).
- [14] L. Bhatt, A. Y. Jiang, E. K. Ko, N. Schnitzer, G. A. Pan, D. F. Segedin, Y. Liu, Y. Yu, Y.-F. Zhao, E. A. Morales, C. M. Brooks, A. S. Botana, H. Y. Hwang, J. A. Mundy, D. A. Muller, and B. H. Goodge, *Resolving Structural Origins for Superconductivity in Strain-Engineered $\text{La}_{0.3}\text{Ni}_{0.2}\text{Sr}_{0.5}\text{O}_{7-x}$ Thin Films* (2025), arXiv:2501.08204 [cond-mat].
- [15] B. Geisler, J. J. Hamlin, G. R. Stewart, R. G. Hennig, and P. J. Hirschfeld, *Fermi surface reconstruction and enhanced spin fluctuations in strained $\text{La}_{0.3}\text{Ni}_{0.2}\text{Sr}_{0.5}\text{O}_{7-x}$ on $\text{LaAlO}_3(001)$ and $\text{SrTiO}_3(001)$* (2025), arXiv:2411.14600 [cond-mat].
- [16] L. C. Rhodes and P. Wahl, *Physical Review Materials* **8**, 044801 (2024).
- [17] Z. Luo, X. Hu, M. Wang, W. Wú, and D.-X. Yao, *Physical Review Letters* **131**, 126001 (2023).
- [18] V. Christiansson, F. Petocchi, and P. Werner, *Physical Review Letters* **131**, 206501 (2023).
- [19] F. Lechermann, J. Gondolf, S. Bötzel, and I. M. Eremin, *Physical Review B* **108**, L201121 (2023).
- [20] J. Yang, H. Sun, X. Hu, Y. Xie, T. Miao, H. Luo, H. Chen, B. Liang, W. Zhu, G. Qu, C.-Q. Chen, M. Huo, Y. Huang, S. Zhang, F. Zhang, F. Yang, Z. Wang, Q. Peng, H. Mao, G. Liu, Z. Xu, T. Qian, D.-X. Yao, M. Wang, L. Zhao, and X. J. Zhou, *Nature Communications* **15**, 4373 (2024).
- [21] P. Puphal, P. Reiss, N. Enderlein, Y.-M. Wu, G. Khalullin, V. Sundaramurthy, T. Priessnitz, M. Knauff, A. Suthar, L. Richter, M. Isobe, P. A. Van Aken, H. Takagi, B. Keimer, Y. E. Suyolcu, B. Wehinger, P. Hansmann, and M. Hepting, *Physical Review Letters* **133**, 146002 (2024).
- [22] L. Wang, Y. Li, S.-Y. Xie, F. Liu, H. Sun, C. Huang, Y. Gao, T. Nakagawa, B. Fu, B. Dong, Z. Cao, R. Yu, S. I. Kawaguchi, H. Kadobayashi, M. Wang, C. Jin, H.-k. Mao, and H. Liu, *Journal of the American Chemical Society* **146**, 7506 (2024).
- [23] Y. Zhang, L.-F. Lin, A. Moreo, T. A. Maier, and E. Dagotto, *Nature Communications* **15**, 2470 (2024).
- [24] T. Xie, M. Huo, X. Ni, F. Shen, X. Huang, H. Sun, H. C. Walker, D. Adroja, D. Yu, B. Shen, L. He, K. Cao, and M. Wang, *Science Bulletin* **69**, 3221 (2024).
- [25] C. Lu, Z. Pan, F. Yang, and C. Wu, *Physical Review Letters* **132**, 146002 (2024).
- [26] X. Chen, J. Choi, Z. Jiang, J. Mei, K. Jiang, J. Li, S. Agrestini, M. Garcia-Fernandez, H. Sun, X. Huang, D. Shen, M. Wang, J. Hu, Y. Lu, K.-J. Zhou, and D. Feng, *Nature Communications* **15**, 9597 (2024).
- [27] Y.-B. Liu, J.-W. Mei, F. Ye, W.-Q. Chen, and F. Yang, *Physical Review Letters* **131**, 236002 (2023).
- [28] H. Oh and Y.-H. Zhang, *Physical Review B* **108**, 174511 (2023).
- [29] Z.-Y. Shao, Y.-B. Liu, M. Liu, and F. Yang, *Physical Review B* **112**, 024506 (2025), arXiv:2501.10409 [cond-mat].
- [30] K. Jiang, Z. Wang, and F.-C. Zhang, *Chinese Physics Letters* **41**, 017402 (2024), arXiv:2308.06771 [cond-mat].
- [31] Y. Gu, C. Le, Z. Yang, X. Wu, and J. Hu, *Physical Review B* **111**, 174506 (2025).
- [32] H. Sakakibara, N. Kitamine, M. Ochi, and K. Kuroki, *Physical Review Letters* **132**, 106002 (2024).
- [33] X.-Z. Qu, D.-W. Qu, J. Chen, C. Wu, F. Yang, W. Li, and G. Su, *Physical Review Letters* **132**, 036502 (2024).
- [34] C. Xia, H. Liu, S. Zhou, and H. Chen, *Nature Communications* **16**, 1054 (2025).
- [35] P. Giannozzi, S. Baroni, N. Bonini, M. Calandra, R. Car, C. Cavazzoni, D. Ceresoli, G. L. Chiarotti, M. Cococcioni, I. Dabo, A. Dal Corso, S. De Gironcoli, S. Fabris, G. Fratesi, R. Gebauer, U. Gerstmann, C. Gougoussis, A. Kokalj, M. Lazzeri, L. Martin-Samos, N. Marzari, F. Mauri, R. Mazzarello, S. Paolini, A. Pasquarello, L. Paulatto, C. Sbraccia, S. Scandolo, G. Sclauzero, A. P. Seitsonen, A. Smogunov, P. Umari, and R. M. Wentzcovitch, *Journal of Physics: Condensed Matter* **21**, 395502 (2009).
- [36] A. A. Mostofi, J. R. Yates, Y.-S. Lee, I. Souza, D. Vanderbilt, and N. Marzari, *Computer Physics Communications* **178**, 685 (2008).
- [37] S. Graser, T. A. Maier, P. J. Hirschfeld, and D. J. Scalapino, *New Journal of Physics* **11**, 025016 (2009).
- [38] C. D. Ling, D. N. Argyriou, G. Wu, and J. J. Neumeier, *Journal of Solid State Chemistry France* **152**, 517 (2000).
- [39] J.-B. de Vaulx, Q. N. Meier, P. Toulemonde, A. Cano, and V. Olevano, *Pressure and strain effects on the $\text{La}_{0.3}\text{Ni}_{0.2}\text{Sr}_{0.5}\text{O}_{7-x}$ d^8 electronic structure of $\text{La}_{0.3}\text{Ni}_{0.2}\text{Sr}_{0.5}\text{O}_{7-x}$* (2025), arXiv:2504.21651 [cond-mat].
- [40] P. Giannozzi, O. Andreussi, T. Brumme, O. Bunau, M. Buongiorno Nardelli, M. Calandra, R. Car, C. Cavazzoni, D. Ceresoli, M. Cococcioni, N. Colonna, I. Carnimeo, A. Dal Corso, S. De Gironcoli, P. Delugas, R. A. DiStasio, A. Ferretti, A. Floris, G. Fratesi, G. Fugallo, R. Gebauer, U. Gerstmann, F. Giustino, T. Gorni, J. Jia, M. Kawamura, H.-Y. Ko, A. Kokalj, E. Küçükbenli, M. Lazzeri, M. Marsili, N. Marzari, F. Mauri, N. L. Nguyen, H.-V. Nguyen, A. Otero-de-la-Roza, L. Paulatto, S. Poncé, D. Rocca, R. Sabatini, B. Santra, M. Schlipf, A. P. Seitsonen, A. Smogunov, I. Timrov, T. Thonhauser, P. Umari, N. Vast, X. Wu, and S. Baroni, *Journal of Physics: Condensed Matter* **29**, 465901 (2017).

- [41] V. I. Anisimov, J. Zaanen, and O. K. Andersen, *Physical Review B* **44**, 943 (1991).
- [42] S. L. Dudarev, G. A. Botton, S. Y. Savrasov, C. J. Humphreys, and A. P. Sutton, *Physical Review B* **57**, 1505 (1998).
- [43] K. F. Garrity, J. W. Bennett, K. M. Rabe, and D. Vanderbilt, *Computational Materials Science* **81**, 446 (2014).
- [44] J. P. Perdew, K. Burke, and M. Ernzerhof, *Physical Review Letters* **77**, 3865 (1996).
- [45] N. Marzari, D. Vanderbilt, A. De Vita, and M. C. Payne, *Physical Review Letters* **82**, 3296 (1999).
- [46] G. Pizzi, V. Vitale, R. Arita, S. Blügel, F. Freimuth, G. Géranton, M. Gibertini, D. Gresch, C. Johnson, T. Koretsune, J. Ibañez-Azpiroz, H. Lee, J.-M. Lihm, D. Marchand, A. Marrazzo, Y. Mokrousov, J. I. Mustafa, Y. Nohara, Y. Nomura, L. Paulatto, S. Poncé, T. Ponweiser, J. Qiao, F. Thöle, S. S. Tsirkin, M. Wierzbowska, N. Marzari, D. Vanderbilt, I. Souza, A. A. Mostofi, and J. R. Yates, *Journal of Physics: Condensed Matter* **32**, 165902 (2020).